Universiteit Leiden
The Netherlands

Visual analytics for spatially resolved omics data at single cell resolution: methods & applications

Somarakis, A.

5

Analysis of multiplexed cellular images in Alzheimer's study

This chapter was adapted from:

B. Kenkhuis*, **A. Somarakis***, L. de Haan, O. Dzyubachyk, M. E. IJsselsteijn, N. F. de Miranda, B. P. Lelieveldt, J. Dijkstra, W. M. van Roon-Mom, T. Höllt, and L. van der Weerd, "Iron loading is a prominent feature of activated microglia in Alzheimer's disease patients ," *Acta Neuropathologica Communications*, vol. 9, no. 1, pp. 1–15, 2021.

* Contributed equally

5.1. ABSTRACT

Brain iron accumulation has been found to accelerate disease progression in amyloid-β(Aβ) positive Alzheimer patients, though the mechanism is still unknown. Microglia have been identified as key players in the disease pathogenesis, and are highly reactive cells responding to aberrations such as increased iron levels. Therefore, using histological methods, multispectral immunofluorescence and an automated in-house developed microglia segmentation and analysis pipeline, we studied the occurrence of iron-accumulating microglia and the effect on its activation state in human Alzheimer brains. We identified a subset of microglia with increased expression of the iron storage protein ferritin light chain (FTL), together with increased Iba1 expression, decreased TMEM119 and P2RY12 expression. This activated microglia subset represented iron-accumulating microglia and appeared morphologically dystrophic. Multispectral immunofluorescence allowed for spatial analysis of FTL$^+$Iba1$^+$-microglia, which were found to be the predominant β-plaque infiltrating microglia. Finally, an increase of FTL$^+$Iba1$^+$-microglia was seen in patients with high β load and Tau load. These findings suggest iron to be taken up by microglia and to influence the functional phenotype of these cells, especially in conjunction with β.

5.2. INTRODUCTION

Alzheimer's disease is the most common cause of dementia, and is defined by the presence of amyloid-β (β) plaques and tau tangles. In addition, the brain's resident innate immune cells, microglia, have been found to be at the centre-stage of the disease, as most identified risk genes are predominantly or even exclusively expressed in microglia [1, 2].

Not only can microglia modulate Alzheimer's disease, but many transcriptomic studies showed microglia to undergo the most pronounced changes in response to pathology. In mice, a subset of responding microglia has been found to lose their homeostatic molecular signature and transition into a so-called 'disease-associated microglia' (DAM) state [3]. In humans, a comparable yet disparate state coined the human Alzheimer microglia (HAM) has been identified [4]. Upregulated genes in these subsets do not only indicate loss of homeostatic function and increased pro-inflammatory activation, but also dysregulated iron-metabolism, manifested via upregulation of the FTL-gene and downregulation of FTH1 and SLC2A11 [4, 5]. FTL encodes the ferritin light chain (FTL) protein, the component of the major iron-storage complex ferritin, responsible for the long term storage of iron. These transcriptomic findings coincide with previously observed ferritin$^+$ microglia in Alzheimer's disease [6, 7]. Though increased iron concentration likely plays a role, the exact link between the two has not yet been established.

Iron accumulation, irrespective of microglial activation, on the other hand, has been reported in disease-affected areas in Alzheimer's disease, using both in-vivo and post-mortem human MRI [8]. Several MRI and histology studies found high correlations between iron accumulation and cortical β and tau spreading [9–11]. Clinically, increased iron concentrations were shown to accelerate cognitive decline in β-positive Alzheimer patients, indicative of a disease-modifying role for iron accumulation [12, 13]. Again, how iron accelerates cognitive deterioration is poorly understood.

Therefore, in this study we aimed to research the possible link between iron accumulation and functionally activated microglia, and finally, its relation with β-plaques.

We performed a comprehensive investigation of iron-accumulating microglia, and first identified that the iron-storage protein FTL, specifically reflected increased iron accumulation in microglia. Secondly, by using multispectral immunofluorescence and an in-house automated cell-analysis pipeline, we found FTL^+ microglia to show significant activation, shown via both downregulation of homeostatic markers TMEM119 and P2RY12 and dystrophic morphology, and to predominantly infiltrate β-plaques. This provides evidence for iron dysregulation as a prominent feature of activated microglia in Alzheimer's disease in humans.

5.3. METHODS

5.3.1. TISSUE ACQUISITION

Brain autopsy tissue of the middle temporal gyrus (MTG) of 12 Alzheimer patients and 9 age-matched controls was collected at the Leiden University Medical Center (LUMC), Netherlands Brain Bank (NBB) and the Normal Aging Brain collection Amsterdam (NABCA). Patients were included based on clinical presentation and diagnosis was confirmed by a neuropathologist. The neuropathologists also evaluates Braak stage, based on Gallyas and Tau immunohistochemistry (IHC), and Thal phase based on Congo Red and Amyloid Beta IHC, in eighteen standard regions, according to the latest international diagnostic criteria [14–16]. Patient demographics are reported in Table 5.1. All material has been collected with written consent from the donors and the procedures have been approved by the Medical Ethical committee of the LUMC and the Amsterdam UMC.

5.3.2. HISTOLOGY AND IMMUNOHISTOCHEMISTRY

Formalin fixed paraffin embedded (FFPE) tissue was serially cut into ten 5-µm-thick and four 10-um-thick sections. Consecutive 10-µm-thick sections were used for histological detection of iron using an enhanced Perl's stain and IHC detection of Ferritin Light Chain (FTL). 5-µm-thick sections were used for staining of the microglia multispectral immunofluorescence (mic-mIF) panel (Table 5.2) to verify expression of FTL in microglia/macrophages (Iba1), look at the activation state of these cells (P2RY12/TMEM119) and study the interaction with Aβ-plaques. Finally, of three subjects, 20-µm-thick sections were obtained for 3D confocal imaging. Step-by-step histological and IHC optimization protocols, together with the imaging parameters, are reported in the Supplementary Methods. A step-by-step mIF protocol and further analysis of the described histological, IHC and mIF staining will be described in the following sections.

5.3.3. MICROGLIA MULTISPECTRAL IMMUNOFLUORESCENCE PANEL

One 5-µm-thick section of each subject was stained with the mic mIF panel with the following protocol, based on a previously described protocol by IJsselsteijn et al. [17]. Sections were deparaffinized with 3×5 min xylene, rinsed twice in 100 % alcohol and subsequently washed with 100% ethanol for 5 min. Endogenous peroxidases were blocked for 20 min in 0.3% H2O2/methanol, after which the slides were rinsed with 70% and 50% alcohol. Heat induced antigen-retrieval was performed by cooking the slides for 10 min in pre-heated citrate (10 mM, pH=6.0) buffer for 10 min. After cooking, excess buffer was removed and slides were cooled for 60 min. Non-specific antibody binding sites

were blocked with blocking buffer (0.1% BSA/PBS+0.05% Tween) for 30 min. Firstly, slides were incubated with anti-TMEM119 (1:250, Sigma Aldrich) diluted in blocking buffer overnight at RT. Slides were washed thrice with PBS and incubated with Poly-HRP secondary antibody for 30 min. Slides were washed again and incubated with the appropriate Opal tertiary antibody (1:100 in amplification diluent, Perkin Elmer) for 60 min, which causes permanent binding of the fluorophore to the antigen site. All subsequent steps are performed in the dark where possible. Finally, the slides are placed back in citrate buffer and cooked in the microwave for 15 min to wash the primary antibody off. The same steps are repeated for anti-P2RY12 (1:2500, Sigma Aldrich). After binding of the two antibodies amplified with Opal, slides are incubated with a primary antibody mix with anti-FTL (1:100, Abcam), anti-Aβ (17–24) (1:250, Biolegend) and anti-Iba1 (1:20, Millipore) antibodies, diluted in blocking buffer, overnight at room temperature. The next day, after three washes with PBS, slides are incubated with a secondary antibody mix of G-a-rIgG A594, G-a-mIgG2b A647 and G-a-mIgG1 CF680 (1:200, ThermoFisher), diluted in 0.1% BSA/BPS. Finally, the slides are washed and incubated with 0.1 µg/mL DAPI (Sigma Aldrich) for 5 min, after which they are mounted with 30 uL Prolong diamond (ThermoFisher).

5.3.4. POST-MORTEM MRI ACQUISITION AND ANALYSIS

MRI data and T2*-w severity scores were obtained from a previous study by Bulk et al. [10], on the same tissue-blocks. In this study, tissue blocks were put in proton-free fluid (Fomblin LC08, Solvay), and scanned at room temperature on a 7 T horizontal-bore Bruker MRI system equipped with a 23 mm receiver coil and Paravision 5.1 imaging software (Bruker Biospin, Ettlingen, Germany). A gradient echo scan was acquired with repetition time=75.0 ms, echo time=33.9 ms, flip angle=25° at 100 µm isotropic resolution with 20 signal averages. Subsequently, cortices were assessed for changes in MRI contrast following a pre-defined scoring system.

5.3.5. IRON-POSITIVE CELL IDENTIFICATION

Whole slide scans of the histochemical iron staining were exported from Philips Intellisite digital Pathology Solution platform (Philips, the Netherlands) and imported into ImageJ. RGB images were converted into 8-bit greyscale images. Subsequently, while blinded for diagnosis, for each subject an optimal threshold was set to include DAB-positive intracellular iron depositions, but exclude extracellular background signal. The cortex of the MTG was delineated and the number of positive cells was determined using the ImageJ particle analyser, with a size threshold of 4–100 pixels. Subject AD5 was excluded from this analysis, as iron-accumulating cells could not be distinguished due to high extracellular iron load.

5.3.6. SINGLE CELL SEGMENTATION

For the presice identification of microglia's cell boundaries the algorithm, stated in Section 2.2, was utilized.

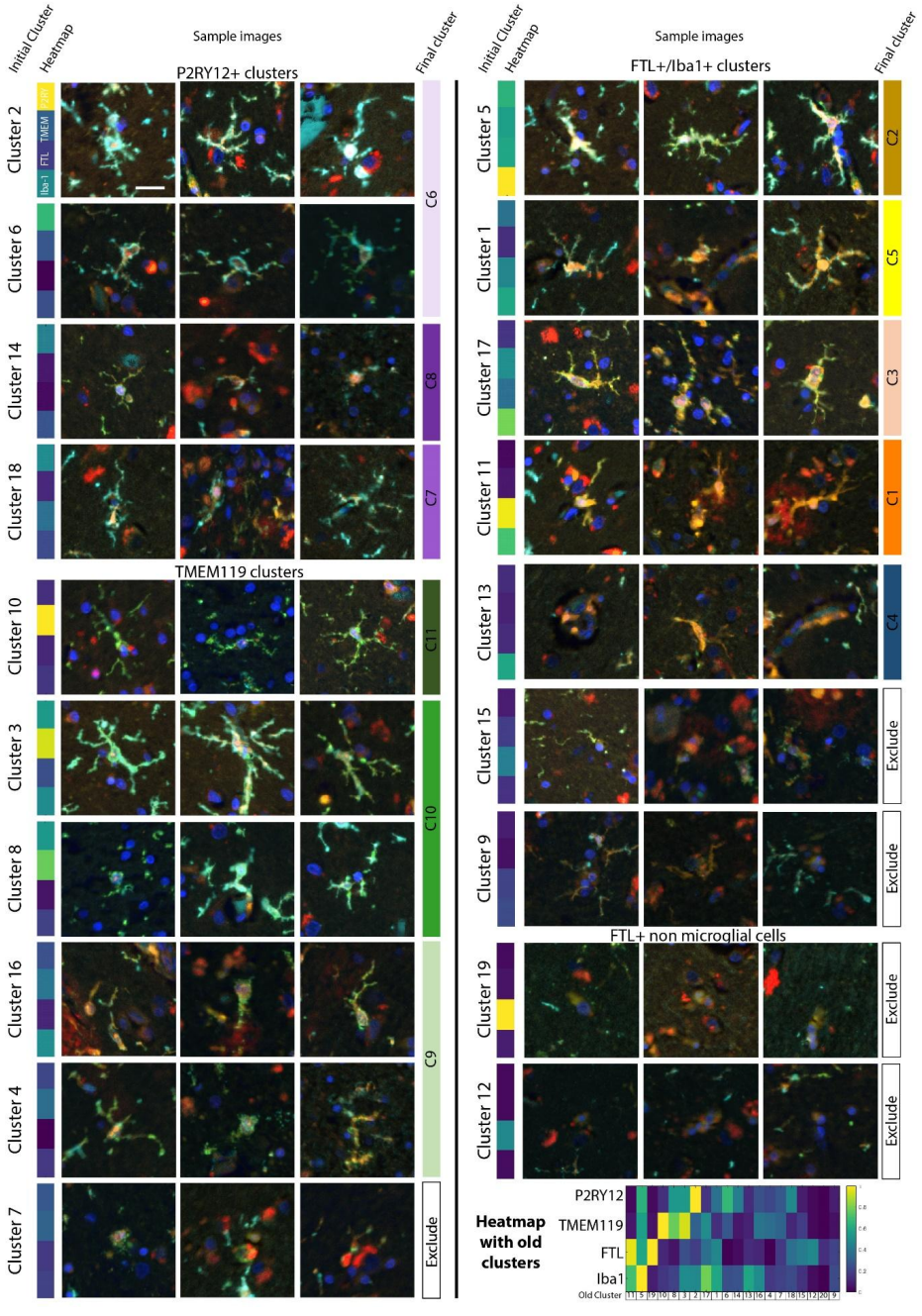

Figure 1: *Sample images of all original clusters, and how they were merged. Scale bar, 20* μm.

5.3.7. CELL PHENOTYPE IDENTIFICATION

Superimposing the segmentation masks onto the component image of all membrane markers, four mean intensity values were extracted for each cell. Afterwards, intensity values were normalized imposing Z-score transformation. For the definition of the different microglia cell types Phenograph [18], an unsupervised clustering method, was utilized. For Phenograph 100 nearest neighbours along with the default parameters were selected, in order to avoid overclustering due to the limited amount of markers. Subsequently, for each Phenograph identified cluster the variability of the single-cell marker expression values was examined (Figure 1) through a violin plot [19] indicating the variation in each cluster, in parallel with their expression patterns as illustrated in the composite images.

5.3.8. ANALYSIS OF CELLULAR PHENOTYPES

The median expression value of each marker for each phenotype was illustrated with a heatmap. The similarities among the identified phenotypes were observed from a t-SNE [20] embedding using the same input as in Phenograph and the default parameters. The t-SNE embedding was coloured according to the cluster of each cell, its cohort or its individual marker expression values [21].

To explore the differences between the Alzheimer patients and controls regarding their phenotypes and their spatial relationship with the Aβ-plaques, an interactive, data-driven pipeline described by [22] was utilized. First, using a version of raincloud plots [22] the phenotypes that exist predominantly in each cohort are identified and consequently, their relative position regarding the Aβ -plaques using a visual query system are explored. For the exploration of the variability in each subject and the validation of our findings, a customized version of the motif glyphs described in our previous work [23] was employed.

5.3.9. STATISTICAL ANALYSIS

Firstly, variables were inspected for being gaussian distributed. If normally-distributed, data plots represent the mean and the standard deviation. For not normally-distributed data, data plots show the median with the corresponding interquartile range. Comparison of two continuous variables was performed using a two-tailed unpaired Student's independent t-test (normally-distributed) or a Mann–Whitney U test (not normally-distributed). Paired normally distributed data were analysed using a two-tailed paired Student's t-test. Bonferroni post-hoc analysis was performed, and a significance level of $P<0.05$ was used. The linear correlation between identified number of cells and different pathological hallmarks was assessed using the Pearson correlation coefficient. All statistical tests were performed using GraphPad Prism (Version 8.00, La Jolla, San Diego, CA, USA).

5.4. RESULTS

5.4.1. FTL$^+$- MICROGLIA REFLECT IRON ACCUMULATING MICROGLIA IN ALZHEIMER'S DISEASE

An enhanced Perl's staining for iron revealed an abundance of iron-positive cells in the cortex of the MTG in Alzheimer's patients. On further inspection, iron-positive cells showed characteristic microglia morphology with a small soma and many thin processes (Figure 2a) and quantification indicated a significant increase of iron-positive cells in

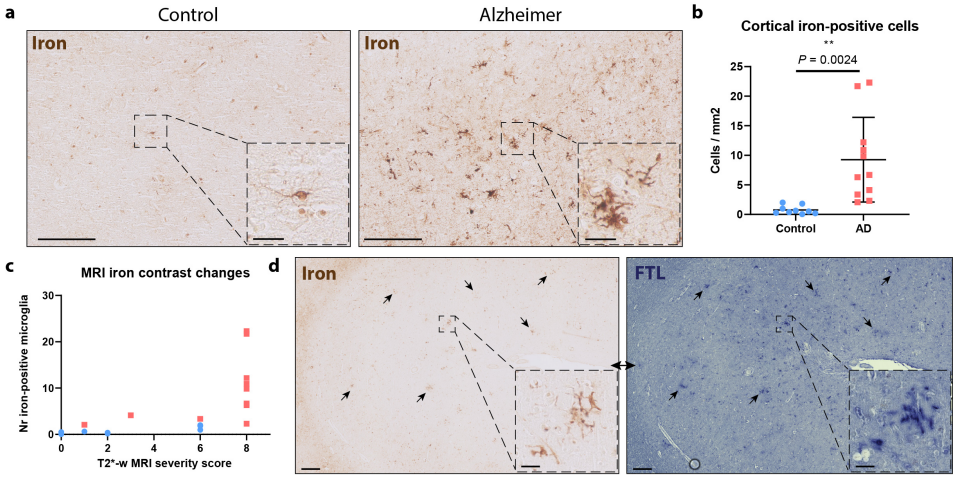

Figure 2: ***Increased iron-positive and corresponding FTL⁺-microglia in Alzheimer's disease.*** *(a) MTG cortex of Alzheimer patients shows increased positivity for iron inside cells with microglial morphology. (b) Significant increase of iron-positive cells in Alzheimer patients (n12) compared to controls (n9)(Mean, Student's t-test). (c) Iron-positive microglia number only increased in cases with severe signal alterations on iron-sensitive T2*-w MRI, reflected by MRI severity score. (d) FTL expression reflects intracellular iron accumulation. Scale overview images, 200 µm. Scale zooms, 30 µm.*

Alzheimer patients compared to controls (P=0.0024; Figure 2b). Additionally, iron-positive cells appeared to cluster in groups, something that was not observed in control patients (Figure 2a). All MTG tissue blocks have also previously been scanned using T2*-w MRI, sensitive for paramagnetic substances such as iron. MRI images were scored based on alterations in signal intensity reflecting overall parenchymal iron accumulation and focal iron depositions, and were published by Bulk et al. [10]. An increase of iron-positive microglia appeared to be only present in cases with the highest MRI severity score, indicating a significant increase of iron-positive microglia only to occur in subjects with a pronounced macroscopic iron-phenotype (Figure 2c). Subsequently we studied the correspondence of iron accumulation with altered expression of the main iron-storage protein ferritin light chain (FTL), as FTL is known to be expressed in microglia and oligodendrocytes, whereas heavy chain ferritin is primarily expressed by neurons in Alzheimer tissue [24]. The Perl's staining and the FTL staining showed a highly similar staining pattern, with focal clusters of cells representing microglia morphology (Figure 2d). Thus, increased expression of the main iron-storage protein FTL appears to reflect iron accumulation in microglial cells.

5.4.2. QUANTITATIVE ANALYSIS ENABLES MICROGLIA PHENOTYPING

To confirm the microglial origin of FTL$^+$ cells, study their activation state and potential interaction with Aβ, we designed the microglia multispectral immunofluorescence (micmIF) panel that can simultaneously detect 6 different markers (Table 5.2). The MTG of 12

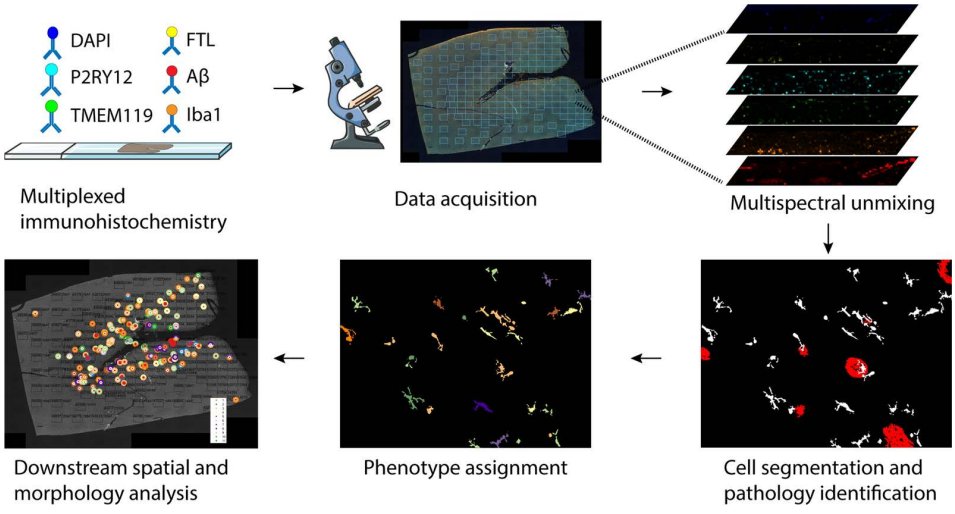

Figure 3: ***Schematic of mic-mIF acquisition and analysis pipeline.***

Alzheimer patients, both of early- and late onset, and 9 control subjects (Table 5.1) was stained and imaged. After image acquisition and multispectral unmixing of the data, images were exported for automated segmentation, phenotyping and spatial analysis (Figure 3). In total, 3149 images (110–236 per subject) were obtained. Multispectral unmixing allowed for simultaneous detection of FTL with the nuclear marker DAPI, TMEM119, P2RY12, Iba1 and Aβ at 0.5×0.5 µm resolution (Figure 4a). TMEM119 and P2RY12 are generally considered homeostatic microglia-specific markers, based on transcriptomic [3], in vitro [25–27] and post-mortem IHC studies [27–29], whose expression decreases when activated. Iba1, on the other hand, is a pan microglia/macrophage marker, which is upregulated upon activation. Finally Aβ stains the characteristic pathological Aβ-plaques that form in the parenchyma of Alzheimer patients. Images were segmented using a targeted in-house segmentation pipeline allowing segmentation of cells with processes (like microglia) in 2D images (Figure 4b; Section 2.2). After segmentation, unsupervised clustering using Phenograph assigned single segmented cells to 20 separate clusters. Following manual evaluation of the unsupervised clusters, 6 clusters were excluded based on non-microglial morphology and/or sub-threshold expression of all microglial markers (TMEM119/P2RY12/Iba1). In addition, three times two clusters were merged based on similarity in protein expression levels and their visual appearance (Figure 1). Exclusion of the non-microglial cells resulted in identification of 69,227 cells, with no significant differences in the number of microglia per mm2 between control and Alzheimer patients in either grey matter (GM) or white matter (WM) (Figure 4c). The remaining 11 clusters (C1–C11) were identified as major microglia phenotype clusters (Figure 4d). Though the 11 different phenotypes clustered on the t-SNE plot, the low degree of separation suggests a rather continuous spectrum of expression of the microglia markers (Figure 4e). The control and Alzheimer patients did cluster together, and the marker-based t-SNE plots already revealed more cells with high TMEM119 and P2RY12 expression in controls, but increased FTL expression in Alzheimer

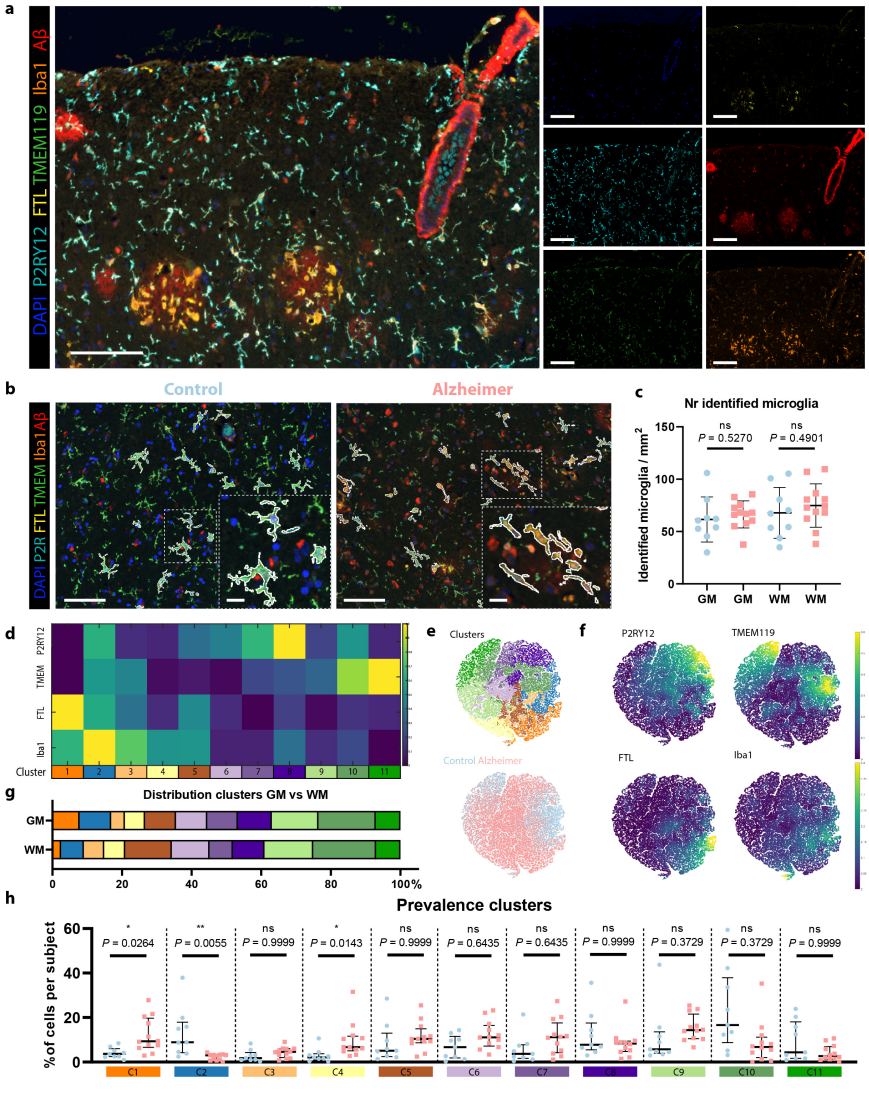

Figure 4: ***Identification of homeostatic and activated Alzheimer-associated microglia clusters.*** *(a) Example of mIF image of an Alzheimer patient. (b) Exemplary images of segmented microglia in a control and an Alzheimer patient. (c) Number of identified cells in the GM and WM of controls (blue; n=9) and Alzheimer patients (red; n=12)(Mean, Student's t-test). (d) Heatmap showing the expression of the four different markers (P2RY12, TMEM119, FTL and Iba1), in the 11 identified microglia clusters. (e) t-SNE plot of all individual cells showing the distinct colour-coded clusters and of control- vs. Alzheimer-patient-derived cells. (f) t-SNE plots colour-coded for intensity of the four individual markers. (g) Distribution of clusters in GM and WM. (h) Prevalence of identified clusters (C1–C11) in individual control (blue; n=9) and Alzheimer patients (red; n=12) (Median, Mann–Whitney U test). Scale bar, 100 μm. Scale bar zooms, 20 μm. GM Grey matter, WM White matter.*

patients (Figure 4f). With regard to anatomical region, only C1 and C2 appeared to be more present in the grey matter (GM), whereas C5 and C6 appeared to be proportionally more present in the white matter (WM) (Figure 4g). Four FTL^+ clusters (C1–C3, C5) were identified, with differing expression levels and co-expression levels of P2RY12, TMEM119 and Iba1 (Figure 4d). Cluster C1 (FTL^+Iba1^+) appeared significantly more present in Alzheimer patients (P=0.0264), while C2 ($P2RY12^+TMEM119^+FTL^+Iba1^+$) was more present in controls (P=0.0055; Figure 4h). FTL^+Iba1^+ clusters lacking either P2RY12 (C3) or TMEM119 (C5) did not differ significantly in prevalence between control and Alzheimer patients. Cluster C4 showed solely Iba1 expression, meaning that this cluster likely also consists of non-resident infiltrating macrophages. Additionally, three $P2RY12^+$ clusters (C6–C8) were identified, with the highest expressing cluster (C8) being more present in controls. The same applied for the $TMEM119^+$ clusters (C9–C11), with C10 and C11 having higher expression and being more present in control patients. These results indicate a small shift of homeostatic microglia positive for P2RY12 and TMEM119 in controls towards activated microglia, with downregulated expression of P2RY12 and TMEM119 in Alzheimer patients. In addition, a specific Alzheimer-associated cluster shows increased expression of a combination of FTL and Iba1.

5.4.3. SPATIAL ANALYSIS OF FTL^+- MICROGLIA CLUSTERS

After cell phenotype identification, all microglia were assessed for proximity to parenchymal Aβ-plaques. For visualization purposes, a second image was created, where infiltrated Aβ-plaques were plotted onto the original image as a 'glyph' (Figure 5a) [23], with the different colours corresponding to the respective cluster of the infiltrating microglia, to analyse which clusters predominantly infiltrated Aβ-plaques. Subsequently, all individual cells represented as cluster-colored dots or the cluster-colored glyphs were plotted back onto the original whole slide image (Figure 5a), to assess differences in cluster composition of microglial Aβ infiltration on a whole-section scale. As expected, quantification showed significantly more identified Aβ-plaques in Alzheimer patients, although some were found in controls as well (P=0.0002; Figure 5b). Furthermore, a higher percentage of the plaques showed microglia infiltration in Alzheimer patients (P=0.013; Figure 5c). Looking at the whole slide distribution, Aβ-plaques were found to be more present in the coronal sulcus rather than the gyrus. This also appeared to be associated with the regional microglia phenotype, as can be seen for the predominantly purple (C6–C8) microglia populating the Aβ-plaque deplete regions (Figure 5d). To quantify the influence of Aβ-plaques on microglia phenotype, we compared all phenotyped microglia (all-mic) with the subset of microglia infiltrating Aβ-plaques (Aβ-mic). Controls showed a slight percental increase of C1 and C5 in Aβ-mic compared to all-mic, and less Aβ-plaque infiltration of $TMEM119^+$ clusters C9–C11 (Figure 5e), though this was based on a limited total number of Aβ-plaques. Alzheimer patients on the other hand, showed a large percental increase of FTL^+ clusters C1 and C3 in the Aβ-mic population (Figure 5e), which was also statistically significant when looking at subject-specific proportional increases (C1: P<0.0001, C3: P=0.0004; Figure 5f, g). While C1 and C3-microglia together make up less than 20% of all-mic, they constitute almost 50% of the Aβ-mic population (Figure 5e). P2RY12+ clusters C6–C8, on the other hand, showed a small contribution to Aβ-mic compared to all-mic (Figure 5e). Finally, not only did C1 and C3 make up the majority of Aβ-mic, but

also when examining the proportions of these individual clusters that directly infiltrated Aβ-plaques, they showed much higher proportion of infiltration than all the other clusters (Figure 5h). A visual example of the C1 and C3-microglia infiltrating an Aβ-plaque on the original mic-mIF images can be found in Figure 5i. All in all, these results suggest Aβ-plaques to be predominantly infiltrated by a specific subset of microglia, characterized

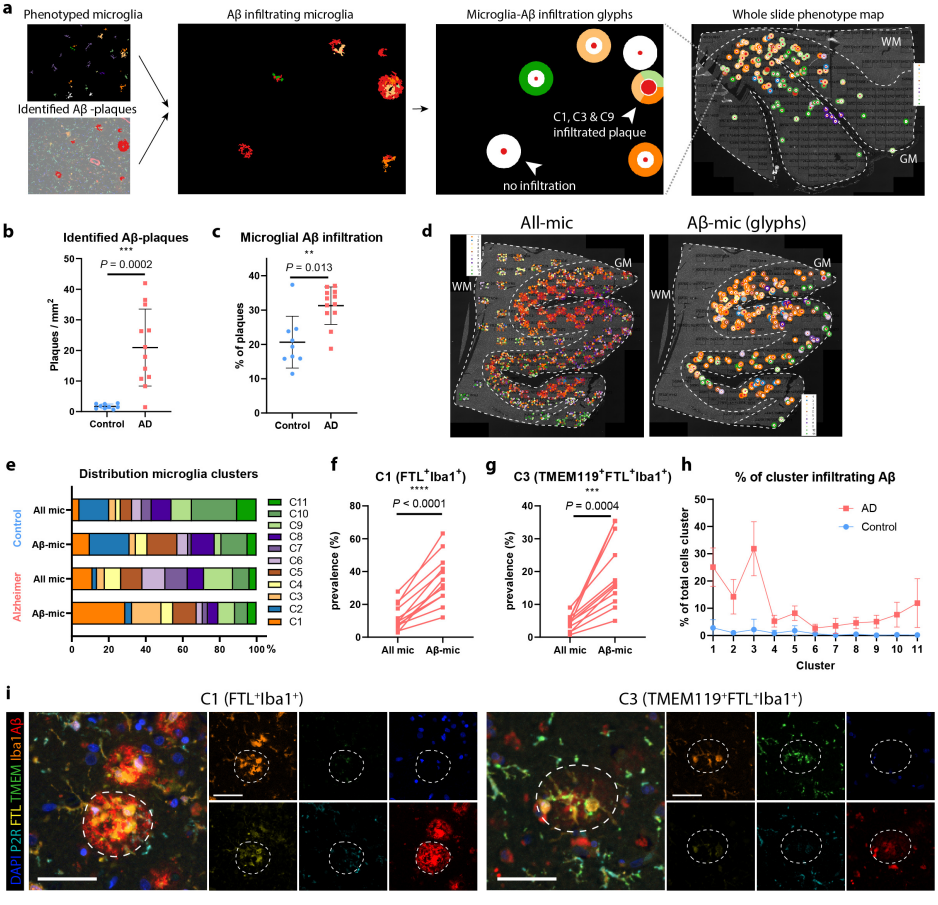

Figure 5: ***FTL⁺-microglia show significant Aβ-plaque infiltration.*** *(a) Schematic of how microglial Aβ-plaque infiltration is studied. Both cells and Aβ-plaques are identified and an interaction map showing 'glyphs' in the colour of the cluster of the infiltrating microglia is created. Subsequently glyphs are plotted back onto the whole slide image to also enable studying the spatial distribution pattern. Number of identified Aβ-plaques (Mean, Student's t-test) (b) and the percentage of microglia infiltrated Aβ-plaques (Mean, Student's t-test) (c) are increased in Alzheimer's disease (n=12) compared to controls (n=9). (d) Microglia clusters differ spatially, depending on the presence of Aβ-plaques in their proximity. (e) Distribution of all-mic clusters compared to Aβ-mic clusters of controls and Alzheimer patients. Comparison of prevalence of all-mic compared to Aβ-mic of C1- (f) and C3-microglia (g) of all individual Alzheimer patients (n=12) (paired Student's t-test). (h) Percentage of all identified clusters infiltrating Aβ-plaques. (i) Representative images of C1 and C3-microglia infiltrating an Aβ-plaque. Scale bar, 50 µm. All mic=all microglia, Aβ-mic=Aβ-plaque infiltrating microglia.*

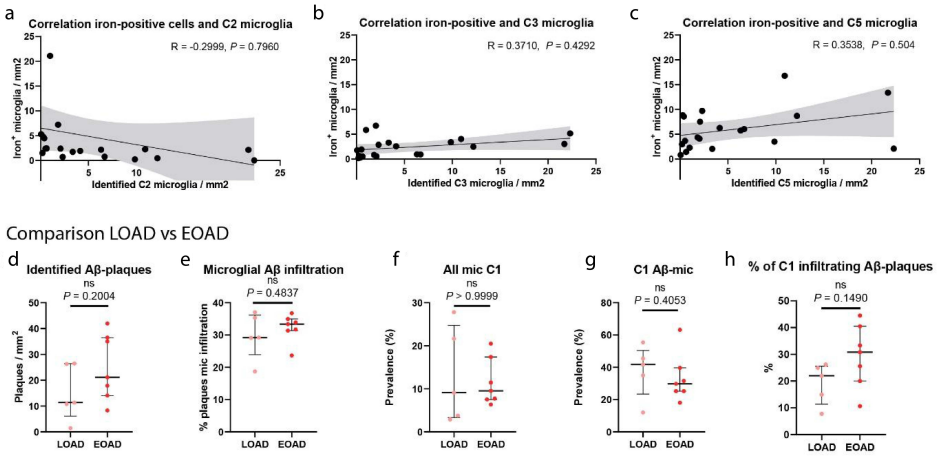

Figure 6: *Correlation of iron+-microglia with C2-microglia (a), C3-microglia (b) and C5-microglia (c) is non-significant (n=20, Pearson coefficient). Comparison between LOAD (n=5) and EOAD (n=7) patients shows no differences in number of identified Aβ-plaques (d), percentage of microglia infiltration (e), prevalence of C1-all-mic (f), prevalence of C1-Aβ-mic (g), and percentage of C1-microglia infiltrating Aβ-plaques (h) (Median, Mann-Whitney U test).*

by increased FTL and Iba1 expression and loss of expression of homeostatic markers P2RY12 or TMEM119 and P2RY12.

5.4.4. CORRELATION OF FTL$^+$-MICROGLIA WITH PATHOLOGY

As already shown in Figure 2d, FTL staining closely followed the enhanced Perl's staining showing microglial iron loading. Therefore, we also checked the correlation of the number of iron-positive microglia with the number of identified microglia of different FTL$^+$ clusters. The number of identified C1 (FTL$^+$Iba1$^+$) microglia correlated well with number of iron–positive-cells (R=0.7601, p=0.0004; Figure 7a), while other FTL$^+$ clusters with lower expression (C2, C3) did not show correlation with number of iron-positive cells (Figure 6a, d). This suggests that it is especially the marked increase of FTL expression found in C1-microglia that reflects substantial iron loading, while moderate FTL expression is also found in non-iron accumulating cells in controls. Although we already found C1-microglia to significantly infiltrate Aβ-plaques, we also checked for its correlation with overall Aβ and Tau load, as assessed by a neuropathologist using Thal stage and Braak stage, respectively. A marked increase of the number of C1-microglia was solely found in high-pathology load subjects with Thal phase V, and Braak stage V/VI (Figure 7b, c), though not all high-pathology load subjects show increase of C1-microglia. C2-microglia were primarily found in controls with low Braak stage I/II and Thal I-II, whereas C3-microglia were present in both controls and Alzheimer patients with varying pathological burdens (Figure 6b, c, e, f). This is in line with the finding that iron-positive microglia were particularly present in Alzheimer patients with advanced iron loading. However, there is lack of Alzheimer patients with intermediate Thal- and Braak-scores, making it impossible to state that an increase of C1-microglia is exclusive to advanced stage disease,

and C3 represents an intermediate state between C2 in controls and C1 in advanced disease. Further investigation into the differences between early-onset Alzheimer's disease (EOAD, onset <65y) patients and late-onset Alzheimer's disease (LOAD, onset >65y) patients, showed no differences in Aβ load, microglia prevalence, or Aβ-infiltration of C1, C2 nor C3 (Figure 6g–q). In addition, we looked at differences between APOE3 and APOE4 carriers, as the latter have been found to have elevated ferritin levels in the CSF [30]. As expected, APOE4 carriers had more Aβ-plaques (Figure 7d), but did not show overall increased microglia infiltration (Figure 7e). Though sample sizes for both groups were small (n=4–6), a trend indicating higher prevalence of C1-microglia in the GM could be observed (P=0.0667; Figure 7f), which was not the case for C2 and C3-microglia (Figure 6r, s) However, no difference was observed when looking at the proportion of Aβ-plaques infiltrated by C1-microglia (Aβ-mic) (P=0.5096; Figure 7g). This suggests that even though a higher percentage of C1-microglia infiltrate Aβ-plaques (P=0.0381; Figure 7h), this is likely due to the increased number of Aβ-plaques present in the APOE4 carriers.

5.4.5. FTL$^+$IBA1$^+$-MICROGLIA HAVE A DYSTROPHIC MORPHOLOGICAL APPEARANCE

Finally, we visually evaluated the morphological appearance of all phenotyped microglia in the same dataset, as this provides additional information about the activation stage of

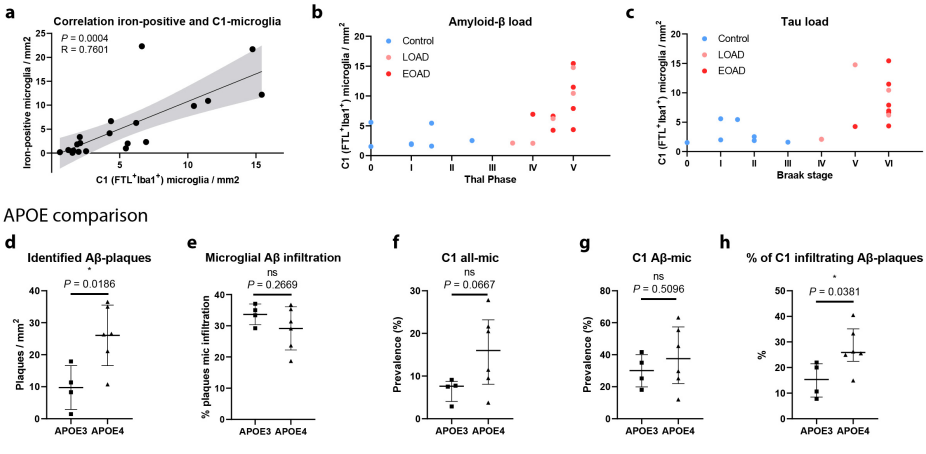

Figure 7: ***C1-microglia (FTL$^+$Iba1$^+$) reflect iron-positive microglia.*** *(a) Number of identified C1-microglia correlates well with number of identified iron-positive microglia (n=20, Pearson coefficient). Increased number of C1-microglia are associated with higher overall Aβ load (Thal) (b) and Tau Load (Braak) (c). Comparison between APOE4 (n=6) vs. APOE3 (n=4) carriers shows increased number of identified Aβ-plaques (d) and similar microglia infiltration (e). Increased prevalence of C1-all-mic (f), no increased proportion of Aβ-plaques infiltrated with C1-mic (Aβ-mic) (g), and significantly increased proportion of C1-microglia infiltrating Aβ-plaques (h). d and e Median, Mann–Whitney U test. Patients AD8 and AD12 were excluded from the APOE comparison analysis as they harbour a familial mutation in the APP and PSEN1 gene, respectively, which could be of more influence than the APOE-genotype.*

the microglia. Two authors (BK and LdH), evaluated the cells according to five distinctive morphological clusters: homeostatic, activated, dystrophic, phagocytic and perivascular macrophages (Figure 8a), based on previously described morphological phenotypes [31]. The parenchyma of controls was predominantly populated by C6–C11-microglia, which consistently expressed TMEM119 and/or P2RY12. These cells presented with homeostatic morphology, showing small circular or oval cell bodies, with thin highly ramified processes and extensive branches (Figure 8b). Morphological appearance therefore appeared to be in line with the homeostatic protein phenotype. Occasionally activated microglia were identified, which have larger cell bodies and noticeably fewer branches and ramifications

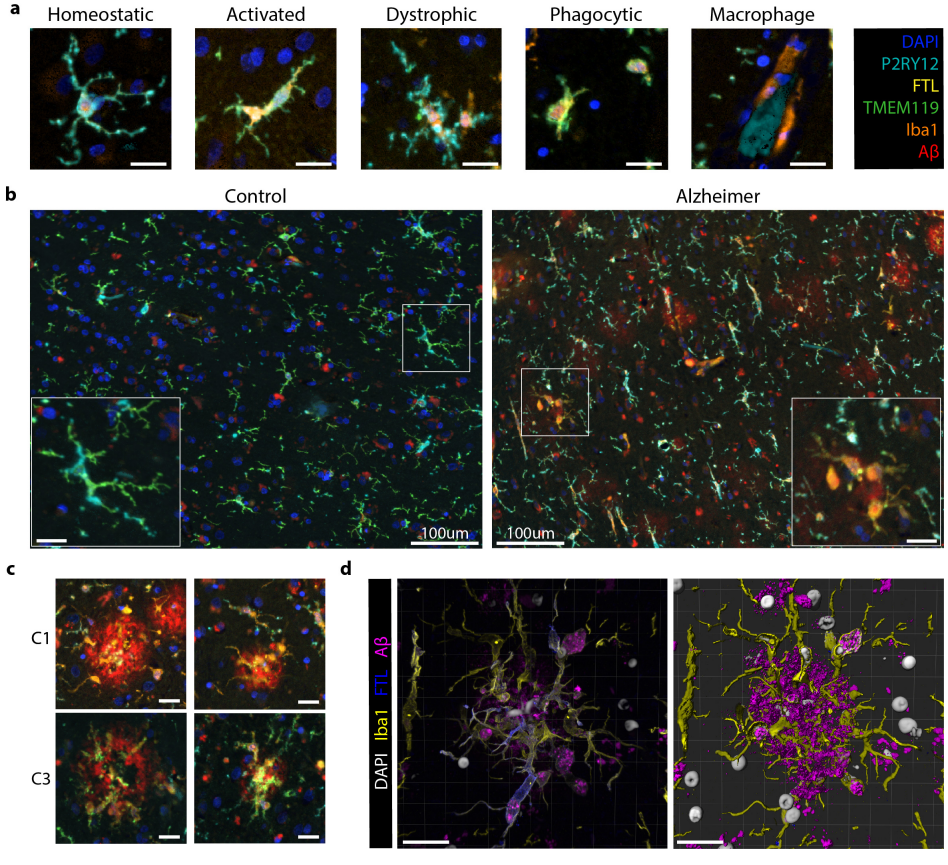

Figure 8: ***C1 and C3-microglia show distinct dystrophic morphology compared to homeostatic control microglia.*** *(a) Representative images of the five different morphological subtypes of microglia: homeostatic, activated, dystrophic, phagocytic and macrophage-like. (b) Controls show predominantly homeostatic and activated microglia, while Alzheimer patients show a variety of homeostatic, activated, phagocytic and dystrophic microglia. (c) Representative images of C1 and C3-microglia surrounding Aβ-plaques showing dystrophic morphology. (d) 3D confocal imaging confirms cytorrhexic appearance of FTL+Iba1+-microglia. Scale bar represents 20 μm unless otherwise stated. Colorcoding for IF-images in 6A-C are according to the box in the top right corner. Colorcoding of 3D confocal images are according to the legend adjacent to the images.*

(especially second degree) (Figure 8a). Activated cells generally showed higher Iba1 and FTL expression and were often phenotyped as C2-microglia (Figure 8a). Microglia in Alzheimer patients, on the other hand, had a much more heterogeneous appearance; homeostatic, activated, dystrophic and phagocytic microglia could all be observed within the coronal sulcus of a single patient (Figure 8b). Though almost all phenotype clusters and morphological clusters could be observed, we focussed on the C1-microglia, as they reflected iron-positive microglia. We found the striking majority of C1-microglia to have a dystrophic morphological appearance. The dystrophic cells show a very distinct phenotype, often with a cloudy or cytorrhexic (fragmentation of the cytoplasm) appearance which results in ill-defined processes (Figure 8a). There is often deramification and the remaining branches show spheroids and fragmentation. Especially microglia (both C1 and C3) infiltrating Aβ plaques showed highly dystrophic morphological characteristics, indicative of an advanced activated/neurodegenerative state (Figure 8c). The dystrophic morphology was also verified using 3D confocal microscopy, which also showed the same cytorrhexic appearance of microglia surrounding the Aβ-plaques (Figure 8d). All in all, the finding of a dystrophic phenotype in C1-microglia was in line with the increased Iba1 and decreased TMEM119 and P2RY12 expression, which accompanied the pronounced FTL expression. They also reflected the morphological appearance of the iron-positive microglia identified on the Perl's staining (Figure 2a).

5.5. DISCUSSION

In this manuscript, we confirmed that increased FTL expression reflects an increase in iron accumulation in microglia in the cortex of Alzheimer patients. Microglia with increased FTL expression also showed higher Iba1 expression, but loss of homeostatic markers TMEM119 and P2RY12, indicative of an activated phenotype. On further investigation this FTL^+Iba1^+ phenotype appeared to be increasingly present in Alzheimer patients and the predominant Aβ-plaque infiltrating microglia phenotype. Morphologically they appeared to be in a dystrophic activation stage.

Firstly, in this study we confirmed that previously identified iron-positive cells in Alzheimer patients [32, 33] are of microglial rather than astrocytic origin, and show high FTL expression. Subsequently, using multispectral fluorescence and unsupervised clustering, we identified several FTL^+ clusters, which were variably present in controls and Alzheimer disease stages. C2-microglia, which displayed positivity for all included microglia markers, were almost exclusively present in control patients. Conversely, C1-microglia (FTL^+Iba1^+) were significantly more present in AD patients, and C3-microglia ($TMEM119^+FTL^+Iba1^+$) were marginally present in either group. Interestingly, both C1 and C3-microglia showed a strong tendency to infiltrate Aβ-plaques. C1-microglia were almost exclusively present in advanced stage Alzheimer patients, whereas C2-microglia were primarily detected in controls (with low Thal/Braak stages), and C3-microglia were variably present across controls and Alzheimer patients of all stages. Regarding the temporal dynamics of these clusters, one could therefore hypothesize that in Alzheimer's disease microglia surround Aβ-plaques and lose P2RY12 expression, as has been observed previously by others (transition from C2 to C3) [28, 34]. As of yet we do not know what the relevance is of the preserved $TMEM119^-$expression. Over time, these microglia take up iron, causing a pronounced increase of FTL expression and loss of TMEM119. This

corresponds to the fact that only C1-microglia appeared to correlate with iron-accumulating microglia. However, our study population is not ideal to dissect the temporal dynamics of these clusters, since the majority of Alzheimer patients showed advanced disease (Braak V/VI) and only two patients showed mild to moderate (Braak III/IV). Future work studying these phenotypes in a larger cohort with a larger range of disease stages would be highly relevant to accurately determine at what stage of the disease C2-microglia prevalence decreases and C1 and C3-microglia prevalence increases.

Several qualitative studies had previously identified increased presence of dystrophic ferritin$^+$ microglia in brain tissue of Alzheimer patients [6, 32, 35, 36]. The dystrophic morphological appearance was also confirmed in this study, though the functional insights of these morphologically defined states remains debatable. Our spatial analysis revealed a strong tendency of FTL$^+$Iba1$^+$ to infiltrate Aβ-plaques; significantly more than can be expected based on prevalence of the cluster itself, and more than any other identified microglia cluster. Although some other studies had already looked into the association of dystrophic ferritin$^+$ microglia with Aβ-plaques [6, 7, 24, 31, 32], results were inconsistent, as none of these studies so far looked into the relative proportion of these microglia in the total population. The importance of this is also stressed in a recent study by Nguyen et al. [37], in which they found an amyloid-responsive microglia (ARM) subset, characterized by CD163, but did not pick up on the Aβ-plaque-infiltrating properties of their identified ferritin$^+$ microglia. Finally, we were able to further characterize iron-positive/FTL$^+$-microglia by analyzing co-expression of several other microglia markers on a single cell level. This revealed that C1-microglia, with the highest FTL protein expression and increased Iba1 expression, showed complete loss of expression of homeostatic markers TMEM119 and P2RY12. Although we acknowledge that our FTL$^+$Iba1$^+$(P2RY12$^-$TMEM119$^-$)-microglia were only characterized using four protein-markers, which is only a fraction compared to the total amount of genes used to define specific transcriptomic states such as the DAM/HAM-states, we do want to highlight the similarities. The DAM/HAM-subsets showed FTL among the highest upregulated genes, with coinciding downregulation of TMEM119 and P2RY12 [3, 4]. Additionally clustering around Aβ-plaques was also reported as a characteristic feature of DAM microglia [3], as is observed for the identified FTL$^+$Iba1$^+$-microglia.

To date, the reason for the observed increase of FTL-expression remains disputed. With FTL being the long-term storage component of ferritin, its expression is likely to be increased in response to increased intracellular labile iron concentrations. Yet, ferritin is also widely recognized as an acute phase reactant and it has also been suggested that microglia upregulate ferritin as a response to exhaustion, caused by the attempt to phagocytose aggregated Aβ [38]. However, our findings show that the identified FTL$^+$Iba1$^+$-microglia closely reflected microglia with high levels of the metal iron, and therefore suggest that the observed increased FTL-expression at least does not merely reflect inflammatory activation or exhaustion, but also increased iron levels. This is in line with a previous study, which found ferritin levels in the CSF to not be associated with an inflammatory response in Alzheimer patients and hypothesized ferritin levels to rather reflect changes in iron associated with tangle and plaque pathology [39].

Why iron increases with age and even more profoundly in neurodegenerative diseases is still largely unknown [8, 40]. It is hypothesized to be caused by several factors including

increased blood–brain barrier permeability and disorganization of the iron-dense myelin sheaths [10, 41, 42]. Alongside a general increase of iron in the parenchyma, iron was also shown to accumulate inside Aβ-plaques [10, 43]. Therefore, a possible hypothesis for why iron is sequestered in microglia surrounding Aβ-plaques, could be that the iron is taken up as byproduct while attempting to phagocytose the Aβ aggregates. Conversely, considering we only found approximately 25% of iron-accumulating C1-microglia to infiltrate Aβ-plaques, iron is more likely sequestered using either DMT1 or Transferrin-receptors and stored inside FTL, in an attempt to mitigate the potentially toxic effects of free iron, which in its free form is suggested to partake in Fenton's reaction to form hydroxyl radicals and cause toxic oxidate stress [42]. When iron is taken up by microglia, it first becomes part of the labile iron pool, where it can produce reactive oxygen species damaging the mitochondria and other cell organelles [44]. Studies performed using peripheral tissue cells showed the non-CNS equivalent of microglia, macrophages, to respond to intracellular iron accumulation by also activating the NLRP3 inflammasome [45]. Accordingly, in vitro and in vivo studies have shown that exposure to a combination of iron and Aβ induces the production of cytokine IL-1β and a switch to glycolytic metabolism in microglia, both of which can be interpreted as NLRP3-inflammasome activation [46, 47]. NLRP3-inflammasome activation in microglia was shown to be able to modify disease progression in two different Alzheimer mouse models [48, 49]. Our data support the in vitro and mouse model evidence that iron and Aβ can act together to accelerate disease progression via microglial inflammasome activation, by showing that in human brain tissue of Alzheimer patients, microglia are exposed to a combination iron and Aβ. Finally, these findings are also in line with recent clinical studies, in which iron was found to act as a potential disease modifier by accelerating deterioration in Alzheimer patients with high Aβ load [12, 13].

Thanks to the possibility to visualize up to six protein markers on the same section using mIF, we could better study the great heterogeneity in microglia phenotype and its spatial relationship with pathology. A limitation of mIF compared to other high-dimensional techniques such as single-cell or imaging mass cytometry is the limited number of markers available to characterize the complex microglial activation states. However, single-cell mass cytometry lacks the spatial component, which is essential when studying the relation with Aβ. Imaging mass cytometry, on the other hand, does capture the spatial distribution, however to date does not enable high-throughput analysis and offers limited resolution. Since microglia have very complicated and variable morphology, solely evaluating protein expression directly surrounding the nucleus is insufficient, and high-resolution images are required for proper segmentation and phenotyping. Secondly, as we are studying relatively rare activated microglia subtypes that will not be present in every ROI or even subject, we required high-throughput quantitative analysis methods. The mIF-mic panel, together with our optimized microglia segmentation pipeline for 2D-images, enabled accurate segmentation and analysis of >60,000 cells to carefully identify the FTL$^+$-microglia in an unbiased fashion.

In this study, we adopted an unsupervised learning approach to generate distinct clusters in our dataset, and avoid bias in the identification in clusters, as can be present in more classical IHC studies. However, as already indicated in the results section, even though distinct clusters were identified, the low degree of separation on the t-SNE mapping and similarity on the associated heatmap, suggest these clusters may be more of a continuum

rather that distinct subsets. This is in line with other transcriptomic and proteomic studies, in which they also showed the microglia clusters to be more of a continuum, even when studying substantially more genes or proteins [5, 50, 51]. However, employment of distinct clusters allows for studying the extreme ends of the continuum of the clusters to find meaningful changes in activation state. Finally, to verify that we were not looking at arbitrary differences in expression levels, we visually checked distinguishability of all independent clusters on the associated immunohistochemical images and merged clusters where this was not possible, as illustrated in Figure 1.

Future studies looking into the effect of iron and Aβ in humanized models such as iPSC-derived microglia would be extremely valuable to decipher the functional effect of this combination, and the influence of Alzheimer-associated genetic risk variants such as APOE. In addition, since microglia, as well as iron accumulation, are shown to be involved in many different neurodegenerative and neuro-immunological disease such as Parkinson's disease and multiple sclerosis, it would be worthwhile looking into this interaction as a common pathway in neurodegeneration. Like for Alzheimer disease, iron could interact with the accumulating protein of interest to affect microglia functioning and consequentially accelerate disease progression.

5.6. CONCLUSION

In summary, we showed that our multispectral immunofluorescence pipeline allowed for accurate identification of specific microglia clusters, and more importantly for the spatial analysis with respect to pathological hallmarks. In this specific study we identified dystrophic $FTL^{+}Iba1^{+}TMEM119^{-}P2RY12^{-}$-microglia to be significantly more present in Alzheimer's disease patient, and to be the predominant Aβ-plaque infiltrating microglia cluster. Finally, in correspondence with the increase of FTL-expression, $FTL^{+}Iba1^{+}$-microglia showed massive iron-loading.

The data that support the findings of this study are available from the corresponding author upon reasonable request.

5.7. ACKNOWLEDGEMENTS

We would like to thank all patients who donated their brain to the Leiden University Medical Center (LUMC), Netherlands Brain Bank (NBB) or the Normal Aging Brain collection Amsterdam (NABCA), and prof. A.J.M. Rozemuller for neuropathological evaluation of the brains. We would also like to thank I.M. Hegeman-Klein for technical assistance with histological and immunohistochemical techniques.

B.Kenkhuis is supported by an MD/PhD-grant from the Leiden University Medical Center. In addition, he has received funding from an early career fellowship from Alzheimer Nederland (WE.15-2018-13) and a Eurolife Scholarship for Early Career researcher. A.Somarakis has received funding through Leiden University Data Science Research Programme. L. van der Weerd received funding from The Netherlands Organization for Scientific Research (NWO) Innovational Research Incentives Scheme (VIDI 864.13.014).

5.8. SUPPLEMENTARY INFORMATION

Table 5.1: ***Patient demographics.*** *** Unknown pathology score. DO = Disease onset. PM = Post-mortem. LOAD = Late onset Alzheimer's disease. EOAD = Early onset Alzheimer's disease.*

	Diagnosis	Sex	DO	Age	Braak	Amyloid load	PM delay	APOE genotype	Familial genetic variant
C1	Control	F		91	2	2/3	03:47	3/3	
C2	Control	M		73	2	1	08:00	3/3	
C3	Control	M		82	**	**	05:30		
C4	Control	F		87	1	0	08:30		
C5	Control	F		72	0	0	07:15		
C6	Control	M		93	**	**	08:30		
C7	Control	M		82	1/2	1/2	07:30		
C8	Control	F		89	3	1/2	06:30	3/4	
C9	Control	F		72	1	1	06:50	3/3	
AD1	LOAD	F	80	88	6	5	04:40	3/4	
AD2	LOAD	M	69	73	5	5	04:45	4/4	
AD3	LOAD	F	>65	82	4	4	04:35	3/4	
AD4	EOAD	F	60	73	6	5	07:17	3/3	
AD5	EOAD	M	61	72	6	5	05:15	3/4	
AD6	EOAD	F	40	67	6	4	04:30	3/4	
AD7	EOAD	F	64	91	6	4/5	04:20	3/3	
AD8	EOAD	M	47	59	5	4/5	05:25	3/3	APP duplication
AD9	LOAD	F	85	90	6	4/5	03:55	2/3	
AD10	EOAD	F	51	70	6	5	04:20	4/4	
AD11	LOAD	F	87	89	4	3-4	04:30	3/3	
AD12	EOAD	F	34	43	6	5	04:15	3/3	PSEN1

Table 5.2: ***Details microglia multispectral immunofluorescence (mic-mIF) panel***

	Staining target	Antibody	Isotype	Antigen retrieval	dilution	Incubation time	Secondary Conjugate
1.	P2RY12	HPA014518, Sigma Aldrich	rIgG	10mM Citrate buffer (pH=6.0)	1:2500	2h	Poly HRP + Opal 520
2.	TMEM119	HPA051870, Sigma Aldrich	rIgG		1:250	ON	Poly HRP + Opal 570
3.	Light Chain Ferritin (FTL)	AB69090, Abcam	rIgG		1:100	ON	G--Rab Alexa 594
4.	A (17–24)	SIG-39220, Biolegend	mIgG2b		1:250	ON	Goat--mIgG2b Alexa 647
5.	Iba1	MABN92, Millipore	mIgG1		1:20	ON	G--mIgG1 CF680
6.	Nucleus, DAPI	D9542-1mg, Sigma Aldrich	n.a.		0.1 µg/ml	5 min	n.a.

Table 5.3: ***Key resources***

Product	Catalogue nr.	Supplier	Dilution
Primary antibodies			
Purified anti--Amyloid	SIG-39220	Bio legend	1:250
Anti-Iba1/AIF1	MABN92	Millipore	1:20
Anti-Ferritin Light Chain (rab)	ab69090	Abcam	1:100
Anti-Ferritin Light Chain (mIgG2a)	SC-74513	Santa Cruz	1:100
Anti-P2RY12	HPA014518	Sigma Aldrich	1:2500
Anti-TMEM119	HPA051870	Sigma Aldrich	1:250
Secondary antibodies			
Opal 520 Reagent Pack	FP1487001KT	Perkin Elmer	1:100
Opal 570 Reagent Pack	FP1488001KT	Perkin Elmer	1:100
Goat anti-Rabbit IgG (H+L), Alexa Fluor 594	A-11037	ThermoFisher	1:200
Goat anti-Mouse IgG2b, Alexa Fluor 647	A-21242	ThermoFisher	1:200
Goat anti-mouse IgG1, CF680	20253	Biotium	1:200
Goat anti-Mouse IgG (H+L), Alexa Fluor 546	A-11003	ThermoFisher	1:200
Goat anti-Rabbit IgG (H+L), Alexa Fluor 546	A-11010	ThermoFisher	1:200
Swine Anti-Rabbit Immunoglobulins/Biotin	E0353	DAKO	1:400
Rabbit anti-Mouse Immunoglobulins/Biotin	E0354	DAKO	1:200
VECTASTAIN Elite ABC-HRP Kit, Peroxidase	PK-6100	Vector Laboraties	n.a.
Extra resources			
BrightVision+ Poly- HRP-Anti Mouse/Rabbit IgG Biotin-free	VWRKDPVO110HRP	Immunologic	n.a.
1X Plus Amplificiation Diluent	FP1498A	Perkin Elmer	n.a.
ProLong Diamond Antifade mountant	P36961	ThermoFisher	n.a.
DAPI	D9542-1mg	Sigma Aldrich	0.1ug/mL
DAB sigma	D5637	Sigma Aldrich	0.5ug/mL

5.8.1. SUPPLEMENTARY METHODS

Histological staining protocol

10-µm-thick sections were used for histochemical iron detection using an enhanced Perl's reaction previously published by Van Duijn et al. [11]. Sections were incubated for 80 min in 1% potassium ferrocyanide, washed three times in 0.1 M phosphate buffer, followed by 100 min incubation in methanol with 0.01 M NaN3 and 0.3% H2O2. Subsequently, sections were washed again and incubated for 80 min in a solution containing 0.025% 3'3-diaminobenzidine-tetrahydrochloride (DAB, Sigma) and 0.005% H2O2 in 0.1 M phosphate buffer. The reaction was stopped by washing with tap water. A consecutive 10-µm-thick section was used for IHC detection of FTL. Sections were deparaffinized with xylene, washed with alcohol and blocked with 0.3% H2O2/methanol for 20 min. Subsequently, they were incubated with FTL (1:100, Santa Cruz) overnight at room temperature and after washing with PBS incubated with anti-rabbit alkaline phosphatase (1:50, Vector) for 1 h. Sections were washed with PBS and incubated with Vector Blue for 20 min in the dark. Finally, they were rinsed and covered with aqua mount.

Brightfield microscopy

Chromogenically stained slides were imaged using a Philips IntelliSite Ultra Fast Scanner (Philips, the Netherlands). Whole slide images could be viewed in 2×–40× magnification using the Philips Intellisite digital Pathology Solution system. Whole slide images were exported at 4× magnification for quantification of number of iron-positive cells. Snapshots of higher magnification were taken directly in the image-viewer.

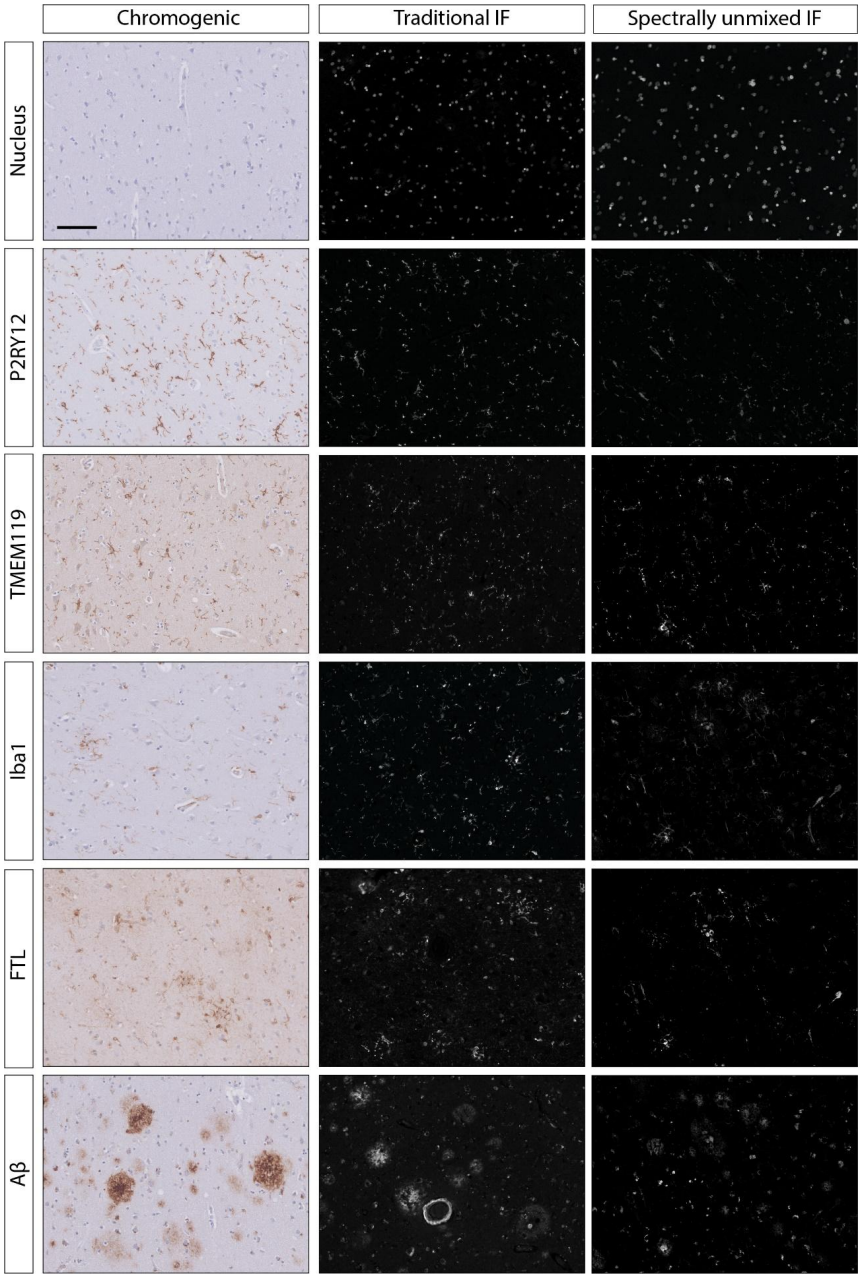

Figure 9: *Sample images of DAB-enhanced, single immunofluorescence and multiplexed immunofluorescence stainings of all antibodies used in our multispectral immunofluorescence panel. Scale bar, 100 μm.*

Antibody validation for multiplexed IHC

The six-colour mic mIF panel (Table 5.2) was created and optimized following a previously described protocol ([17]). Individual antibody conditions were optimized using single IHC and IF. Firstly, individual antibodies were tested with chromogenic and fluorescent detection for optimal antibody concentration and antigen retrieval method with the following protocol. 5-µm-thick FFPE tissue sections were deparaffinized with xylene, washed with alcohol and endogenous peroxidase was blocked by incubating in 0.3% H202 in methanol for 20 min. Antigen retrieval was performed with either citrate buffer (10 mM, pH = 6.0) or EDTA buffer (10 mM, pH 9.0). After cooling, the sections were blocked with 0.1% BSA/PBS with 0.05% Tween for 30 min and incubated with primary antibody diluted in blocking buffer in a range of concentrations overnight at room temperature. For chromogenic detection, the slides were washed with PBS and incubated with Sw-a-Rb/biotin (1:400, Dako) or Sw-a-Mouse/biotin (1:200, DAKO) for 60 min, followed by 30 min incubation with VECTAstain elite ABC. Chromogenic substrate was developed with 0.05% DAB (Sigma) with 0.005% H2O2 for 10 min. The reaction was stopped with tap water, after which the sections were counterstained with haematoxylin for 5 min and mounted with micromount. For fluorescent detection, slides were incubated with the appropriate Alexa 546 fluorophore (1:200, ThermoFisher) for 1 hour. Subsequently, the slides were incubated with 0.1 µg/mL DAPI (Sigma) for 5 min and mounted with prolong diamond (ThermoFisher). After individual antibody testing, antibodies were combined to test the viability for multiplexed immunofluorescence. The full protocol described in Section 5.3.9 was performed for 7 slides of one control and one AD subject. One slide of each was incubated with all primary antibodies. For each of the other slides the exact same protocol was performed, but only 1 out of the 6 primary antibodies was added in the primary incubation step. These slides were used to analyse the fluorescent spectrum of the individual fluorophores on our slides, which are subsequently used to un-mix the 6 different spectra. To verify specificity, the extracted signal was compared with single immunofluorescence (Figure 9).

Multispectral microscopy and image-acquisition

Mic-mIF-stained tissue slides were scanned at 4× magnification using the Vectra 3.0 Automated Quantitative Pathology Imaging system (PerkinElmer). Following whole slide scanning, a 50% and 25% ROI grid was placed on the cortex and white matter, respectively. For each ROI, high-resolution 20× magnification images are obtained of all subjects. Spectral separation of the 6 individual dyes was performed automatically using InForm Cell Analysis software (PerkinElmer), using spectral libraries obtained with single-marker IF detection of the different fluorophores. In total, six different raw component images of the extracted spectra were exported from Inform for further analysis.

Confocal microscopy

20 µm sections were imaged using an Andor Dragonfly 200 spinning disk confocal system (Andor, Oxford Instruments). Sections were stained with DAPI, Alexa 488, Alexa 546 and Alexa 647, which were imaged with a 405 nm, 488 nm, 561 nm and 637 nm laser respectively. Subsequently images were exported and processed using Imaris (Bitplane, Oxford instruments). First, a Gaussian filter was applied to all channels, after which snapshots of the reconstructed 3D projection were taken.

References

[1] I. E. Jansen, J. E. Savage, K. Watanabe, J. Bryois, D. M. Williams, and S. Steinberg, "Genome-wide meta-analysis identifies new loci and functional pathways influencing alzheimer's disease risk," *Nat Genet*, vol. 51, 2019.

[2] J. C. Lambert, C. A. Ibrahim-Verbaas, D. Harold, A. C. Naj, R. Sims, and C. Bellenguez, "Meta-analysis of 74,046 individuals identifies 11 new susceptibility loci for alzheimer's disease," *Nat Genet*, vol. 45, 2013.

[3] H. Keren-Shaul, A. Spinrad, A. Weiner, O. Matcovitch-Natan, R. Dvir-Szternfeld, and T. K. Ulland, "A unique microglia type associated with restricting development of alzheimer's disease," *Cell*, vol. 169, 2017.

[4] H. Mathys, J. Davila-Velderrain, Z. Peng, F. Gao, S. Mohammadi, and J. Z. Young, "Single-cell transcriptomic analysis of alzheimer's disease," *Nature*, vol. 570, 2019.

[5] Y. Zhou, W. M. Song, P. S. Andhey, A. Swain, T. Levy, and K. R. Miller, "Human and mouse single-nucleus transcriptomics reveal trem2-dependent and trem2-independent cellular responses in alzheimer's disease," *Nat Med*, vol. 26, 2020.

[6] K. O. Lopes, D. L. Sparks, and W. J. Streit, "Microglial dystrophy in the aged and alzheimer's disease brain is associated with ferritin immunoreactivity," *Glia*, vol. 56, 2008.

[7] I. Grundke-Iqbal, J. Fleming, Y. C. Tung, H. Lassmann, K. Iqbal, and J. G. Joshi, "Ferritin is a component of the neuritic (senile) plaque in alzheimer dementia," *Acta Neuropathologica*, vol. 81, 1990.

[8] A. Damulina, L. Pirpamer, M. Soellradl, M. Sackl, C. Tinauer, and E. Hofer, "Cross-sectional and longitudinal assessment of brain iron level in alzheimer disease using 3-t mri," *Radiology*, vol. 296, 2020.

[9] N. Spotorno, J. Acosta-Cabronero, E. Stomrud, B. Lampinen, O. T. Strandberg, and D. Westen, "Relationship between cortical iron and tau aggregation in alzheimer's disease," *Brain*, vol. 143, 2020.

[10] M. Bulk, B. Kenkhuis, L. M. Graaf, J. J. Goeman, R. Natté, and L. Weerd, "Post-mortem t2*- weighted mri imaging of cortical iron reflects severity of alzheimer's disease," *J Alzheimer's Dis*, vol. 65, 2018.

[11] S. Duijn, M. Bulk, S. G. Duinen, R. J. A. Nabuurs, M. A. Buchem, and L. Weerd, "Cortical iron reflects severity of alzheimer's disease," *J Alzheimer's Dis*, vol. 60, 2017.

[12] S. Ayton, A. Fazlollahi, P. Bourgeat, P. Raniga, A. Ng, and Y. Y. Lim, "Cerebral quantitative susceptibility mapping predicts amyloid--related cognitive decline," *Brain*, vol. 140, 2017.

[13] S. Ayton, Y. Wang, I. Diouf, J. A. Schneider, J. Brockman, and M. C. Morris, "Brain iron is associated with accelerated cognitive decline in people with alzheimer pathology," *Mol Psychiatry*, vol. 66, 2019.

[14] H. Braak and E. Braak, "Neuropathological stageing of alzheimer-related changes," *Acta Neuropathologica*, vol. 66, 1991.

[15] H. Braak and E. Braak, "Staging of alzheimer's disease-related neurofibrillary changes," *Neurobiol Aging Neurobiol Aging*, vol. 16, 1995.

[16] B. T. Hyman, C. H. Phelps, T. G. Beach, E. H. Bigio, N. J. Cairns, and M. C. Carrillo, "National institute on aging-alzheimer's association guidelines for the neuropathologic assessment of alzheimer's disease," *Alzheimer's Dement NIH Public Access*, vol. 8, 2012.

[17] M. E. Ijsselsteijn, T. P. Brouwer, Z. Abdulrahman, E. Reidy, A. Ramalheiro, A. M. Heeren, A. Vahrmeijer, E. S. Jordanova, and N. F. de Miranda, "Cancer immunophenotyping by seven-colour multispectral imaging without tyramide signal amplification," *The Journal of Pathology: Clinical Research*, vol. 5, pp. 3–11, 2019.

[18] J. Levine, E. Simonds, S. Bendall, K. Davis, E. ad D. Amir, M. Tadmor, O. Litvin, H. Fienberg, A. Jager, E. Zunder, R. Finck, A. Gedman, I. Radtke, J. Downing, D. Pe'er, and G. Nolan, "Data-driven phenotypic dissection of aml reveals progenitor-like cells that correlate with prognosis," *Cell*, vol. 162, no. 1, pp. 184–197, 2015.

[19] J. L. Hintze and R. D. Nelson, "Violin plots: A box plot-density trace synergism," *The American Statistician*, vol. 52, no. 2, pp. 181–184, 1998.

[20] L. v. d. Maaten and G. Hinton, "Visualizing data using t-sne," *Journal of machine learning research*, vol. 9, no. Nov, pp. 2579–2605, 2008.

[21] T. Höllt, N. Pezzotti, V. van Unen, F. Koning, E. Eisemann, B. P. F. Lelieveldt, and A. Vilanova, "Cytosplore: Interactive immune cell phenotyping for large single-cell datasets," *Computer Graphics Forum (Proceedings of EuroVis)*, vol. 35, no. 3, pp. 171–180, 2016.

[22] A. Somarakis, M. E. Ijsselsteijn, S. J. Luk, B. Kenkhuis, N. F. C. C. de Miranda, B. P. F. Lelieveldt, and T. Höllt, "Visual cohort comparison for spatial single-cell omics-data," *IEEE Transactions on Visualization and Computer Graphics*, vol. 27, no. 2, pp. 733–743, 2021.

[23] A. Somarakis, V. van Unen, F. Koning, B. P. Lelieveldt, and T. Höllt, "ImaCytE: visual exploration of cellular microenvironments for imaging mass cytometry data," *IEEE Transactions on Visualization and Computer Graphics*, vol. 27, no. 1, pp. 98–110, 2021.

[24] M. Meadowcroft, J. Connor, and Q. Yang, "Cortical iron regulation and inflammatory response in alzheimer's disease and appswe/ps1e9 mice: a histological perspective," *Frontiers in Neuroscience*, vol. 9, p. 255.

[25] P. Banerjee, E. Paza, E. M. Perkins, O. G. James, B. Kenkhuis, A. F. Lloyd, K. Burr, D. Story, D. Yusuf, X. He, R. Backofen, O. Dando, S. Chandran, and J. Priller, "Generation of pure monocultures of human microglia-like cells from induced pluripotent stem cells," *Stem Cell Research*, vol. 49, p. 102046, 2020.

[26] T. A. van Wageningen, E. Vlaar, G. Kooij, C. A. M. Jongenelen, J. J. G. Geurts, and A. M. van Dam, "Regulation of microglial TMEM119 and P2RY12 immunoreactivity in multiple sclerosis white and grey matter lesions is dependent on their inflammatory environment," *Acta Neuropathologica Communications*, vol. 7, no. 1, p. 206, 2019.

[27] M. L. Bennett, F. C. Bennett, S. A. Liddelow, B. Ajami, J. L. Zamanian, N. B. Fernhoff, S. B. Mulinyawe, C. J. Bohlen, A. Adil, A. Tucker, I. L. Weissman, E. F. Chang, G. Li, G. A. Grant, M. G. Hayden Gephart, and B. A. Barres, "New tools for studying microglia in the mouse and human cns," *Proceedings of the National Academy of Sciences*, vol. 113, no. 12, pp. E1738–E1746, 2016.

[28] A. Mildner, H. Huang, J. Radke, W. Stenzel, and J. Priller, "P2y 12 receptor is expressed on human microglia under physiological conditions throughout development and is sensitive to neuroinflammatory diseases," *Glia*, vol. 65, pp. 375–387.

[29] T. Zrzavy, S. Hametner, I. Wimmer, O. Butovsky, H. L. Weiner, and H. Lassmann, "Loss of 'homeostatic' microglia and patterns of their activation in active multiple sclerosis," *Brain*, vol. 140, no. 7, pp. 1900–1913, 2017.

[30] S. Ayton, N. G. Faux, A. I. Bush, and A. D. N. Initiative, "Ferritin levels in the cerebrospinal fluid predict alzheimer's disease outcomes and are regulated by apoe," *Nature Communications*, vol. 6, no. 1, p. 6760, 2015.

[31] W. J. Streit, Q. S. Xue, J. Tischer, and I. Bechmann, "Microglial pathology," *Acta Neuropathologica Communications*, vol. 2, p. 142, 2014.

[32] J. R. Connor, S. L. Menzies, S. M. St. Martin, and E. J. Mufson, "A histochemical study of iron, transferrin, and ferritin in alzheimer's diseased brains," *Journal of Neuroscience Research*, vol. 31, no. 1, pp. 75–83, 1992.

[33] M. M. Zeineh, Y. Chen, H. H. Kitzler, R. Hammond, H. Vogel, and B. K. Rutt, "Activated iron-containing microglia in the human hippocampus identified by magnetic resonance imaging in alzheimer disease," *Neurobiol Aging*, vol. 36, pp. 2483–2500, 2015.

[34] D. G. Walker, T. M. Tang, A. Mendsaikhan, I. Tooyama, G. E. Serrano, L. I. Sue, T. G. Beach, and L.-F. Lue, "Patterns of Expression of Purinergic Receptor P2RY12, a Putative Marker for Non-Activated Microglia, in Aged and Alzheimer's Disease Brains," vol. 21, no. 2, 2020.

[35] Y. Kaneko, T. Kitamoto, J. Tateishi, and K. Yamaguchi, "Ferritin immunohistochemistry as a marker for microglia," *Acta Neuropathologica*, vol. 79, no. 2, pp. 129–136, 1989.

[36] K. Jellinger, W. Paulus, I. Grundke-Iqbal, P. Riederer, and M. B. H. Youdim, "Brain iron and ferritin in parkinson's and alzheimer's diseases," *Journal of Neural Transmission - Parkinson's Disease and Dementia Section*, vol. 2, no. 4, pp. 327–340, 1990.

[37] A. T. Nguyen, K. Wang, G. Hu, X. Wang, Z. Miao, J. A. Azevedo, E. Suh, V. M. Van Deerlin, D. Choi, K. Roeder, M. Li, and E. B. Lee, "Apoe and trem2 regulate amyloid-responsive microglia in alzheimer's disease," *Acta Neuropathologica*, vol. 140, no. 4, pp. 477–493, 2020.

[38] W. J. Streit, H. Braak, K. Del Tredici, J. Leyh, J. Lier, H. Khoshbouei, C. Eisenlöffel, W. Müller, and I. Bechmann, "Microglial activation occurs late during preclinical alzheimer's disease," *Glia*, vol. 66, no. 12, pp. 2550–2562, 2018.

[39] S. Ayton, S. Janelidze, B. Roberts, S. Palmqvist, P. Kalinowski, I. Diouf, A. A. Belaidi, E. Stomrud, A. I. Bush, and O. Hansson, "Acute phase markers in csf reveal inflammatory changes in alzheimer's disease that intersect with pathology, apoe 4, sex and age," *Progress in Neurobiology*, vol. 198, p. 101904, 2021.

[40] J. Acosta-Cabronero, M. J. Betts, A. Cardenas-Blanco, S. Yang, and P. J. Nestor, "In vivo mri mapping of brain iron deposition across the adult lifespan," *Journal of Neuroscience*, vol. 36, no. 2, pp. 364–374, 2016.

[41] A. J. Farrall and J. M. Wardlaw, "Blood–brain barrier: ageing and microvascular disease—systematic review and meta-analysis," *Neurobiol Aging*, vol. 25, pp. 337–352, 2009.

[42] R. J. Ward, F. A. Zucca, J. H. Duyn, R. R. Crichton, and L. Zecca, "The role of iron in brain ageing and neurodegenerative disorders," *The Lancet Neurology*, vol. 13, no. 10, pp. 1045–1060, 2014.

[43] R. J. Nabuurs, I. Hegeman, R. Natté, S. G. van Duinen, M. A. van Buchem, L. van der Weerd, and A. G. Webb, "High-field mri of single histological slices using an inductively coupled, self-resonant microcoil: application to ex vivo samples of patients with alzheimer's disease," *NMR in Biomedicine*, vol. 24, no. 4, pp. 351–357, 2011.

[44] S. J. Dixon and B. R. Stockwell, "The role of iron and reactive oxygen species in cell death," *Nature Chemical Biology*, vol. 10, no. 1, pp. 9–17, 2014.

[45] K. Nakamura, T. Kawakami, N. Yamamoto, M. Tomizawa, T. Fujiwara, T. Ishii, H. Harigae, and K. Ogasawara, "Activation of the nlrp3 inflammasome by cellular labile iron," *Experimental Hematology*, vol. 44, no. 2, pp. 116–124, 2016.

[46] A. McIntosh, V. Mela, C. Harty, A. M. Minogue, D. A. Costello, C. Kerskens, and M. A. Lynch, "Iron accumulation in microglia triggers a cascade of events that leads to altered metabolism and compromised function in app/ps1 mice," *Brain Pathology*, vol. 29, no. 5, pp. 606–621, 2019.

[47] I. C. Nnah, C.-H. Lee, and M. Wessling-Resnick, "Iron potentiates microglial interleukin-1β secretion induced by amyloid-β," *Journal of neurochemistry*, vol. 154, no. 2, pp. 177–189, 2020.

[48] C. Ising, C. Venegas, S. Zhang, H. Scheiblich, S. V. Schmidt, A. Vieira-Saecker, S. Schwartz, S. Albasset, R. M. McManus, D. Tejera, A. Griep, F. Santarelli, F. Brosseron, S. Opitz, J. Stunden, M. Merten, R. Kayed, D. T. Golenbock, D. Blum, E. Latz, L. Buée, and M. T. Heneka, "Nlrp3 inflammasome activation drives tau pathology," *Nature*, vol. 575, no. 7784, pp. 669–673, 2019.

[49] M. T. Heneka, M. P. Kummer, A. Stutz, A. Delekate, S. Schwartz, A. Vieira-Saecker, A. Griep, D. Axt, A. Remus, T.-C. Tzeng, E. Gelpi, A. Halle, M. Korte, E. Latz, and D. T. Golenbock, "Nlrp3 is activated in alzheimer's disease and contributes to pathology in app/ps1 mice," *Nature*, vol. 493, no. 7434, pp. 674–678, 2013.

[50] R. Sankowski, C. Böttcher, T. Masuda, L. Geirsdottir, E. Sindram, T. Seredenina, A. Muhs, C. Scheiwe, M. J. Shah, D. H. Heiland, *et al.*, "Mapping microglia states in the human brain through the integration of high-dimensional techniques," *Nature neuroscience*, vol. 22, no. 12, pp. 2098–2110, 2019.

[51] C. Böttcher, S. Schlickeiser, M. A. M. Sneeboer, D. Kunkel, A. Knop, and E. Paza, "Human microglia regional heterogeneity and phenotypes determined by multiplexed single-cell mass cytometry," *Nat Neurosci*, vol. 22, 2019.